Chemical Science

Accepted Manuscript

This article can be cited before page numbers have been issued, to do this please use: M. Gigantino, H. Moise, V. Haribal, A. Tong, J. Shen, D. Saad, J. Fishman, A. J.H. Nelson, H. Voorhis, E. Sun, A. R. Brandt, R. Gupta, A. Majumdar and M. Cargnello, *Chem. Sci.*, 2025, DOI: 10.1039/D5SC00768B.

ROYAL SOCIETY OF CHEMISTRY

rsc.li/chemical-science

View Article Online
DOI: 10.1039/D5SC00768B

Oxidant-assisted methane pyrolysis

Marco Gigantino,[1,#] Henry Moise,[1,#] Vasudev Haribal,[2] Andrew Tong,[2] Jian Ping Shen,[2] Dimitri Saad,[3] Jacob Fishman[1], Alexander Nelson[1], Harry Voorhis[1], Eddie Sun[4], Adam Brandt,[3] Raghubir Gupta,[2] Arun Majumdar[4,5] and Matteo Cargnello[1,6,*]

[1] *Department of Chemical Engineering, Stanford University, Stanford, CA 94305, USA.*

[2] *Susteon Inc., Cary, NC 27513, USA*

[3] *Department of Energy Science & Engineering, Stanford University, Stanford, CA 94305, USA.*

[4] *Department of Mechanical Engineering, Stanford University, Stanford, CA 94305, USA.*

[5] *Precourt Institute for Energy, Stanford University, Stanford, CA 94305, USA*

[6] *SUNCAT Center for Interface Science and Catalysis, Stanford University, Stanford, CA 94305, USA.*

[#] *These authors contributed equally.*

† Electronic supplementary information (ESI) available.

** Corresponding author e-mail: mcargnello@stanford.edu*

Abstract

Methane pyrolysis has been proposed as a cost-competitive route to produce low-CO_2-emissions hydrogen that can utilize today's infrastructure to supply feedstock and manage waste, and thereby be rapidly scalable. However, this process faces challenges such as catalyst deactivation and carbon build-up that hinder its large-scale implementation. Pyrolysis is usually conducted in the absence of oxidizers to avoid combustion products such as CO_2. Here, we demonstrate that the addition of small concentrations of an oxidant to a methane pyrolysis reaction on Fe-based catalysts prevented catalyst deactivation and increased the net production of carbon and hydrogen. Methane pyrolysis in the presence of a small amount of CO_2 demonstrated a twofold increase in carbon yield and a 7.5-fold increase in hydrogen concentration in the effluent compared to that of a pure methane feed during 1 h operation in a fluidized bed reactor at 750 °C. A similar beneficial effect was observed by adding small amounts of H_2O in the feed. We provide evidence that the cyclic formation and decomposition of an iron carbide catalyst phase allowed for increased methane decomposition and significant carbon removal from the catalyst surface, thus increasing carbon and hydrogen yields. A similar result was obtained for Ni- and Co-based catalysts.

Introduction

View Article Online
DOI: 10.1039/D5SC00768B

While there are sufficient geological reserves of coal, oil, and natural gas (NG) to fuel our society for at least the next century, the environmental consequences associated with the continued emissions of CO_2 and other greenhouse gases (GHG) into the atmosphere have spurred a global initiative for an earlier transition away from them(1). The adoption of carbon taxes, emissions-based penalties and/or financial incentives for GHG-free approaches may allow for more sustainable energy sources like GHG-free hydrogen to compete in the market with fossil fuels(2). Additionally, advancements in technologies, such as more efficient hydrogen production methods and the co-production of valuable commodities like carbon, could further reduce costs and enhance hydrogen's competitiveness as a cleaner energy source(3).

Currently, hydrogen is a vital chemical intermediate for many industrial sectors crucial to the global economy, including ammonia production and hydrocarbon refining(4). Low-cost, low-carbon hydrogen is needed to support crucial chemical processes for many decades to come. At the same time, it has the potential to scale as an advanced fuel and meet the energy demands of the primary and secondary economic sectors(5). Hydrogen can be utilized for power generation with zero direct emissions. Its production, however, is currently highly carbon intensive.

The most cost-effective route to produce hydrogen today is through the partial oxidation of fossil hydrocarbons via steam reforming or autothermal reforming followed by water-gas shift (WGS). Reforming reactors supply as much as 95% of global hydrogen demand today but do so with associated process emissions in the range of 9-12 kg CO_2/kg H_2(6).

The combination of steam methane reforming (SMR) ($CH_4 + H_2O \rightleftharpoons 3H_2 + CO$, $\Delta H_{rxn,298K}$ = 69 kJ/mol H_2) with WGS ($CO + H_2O \rightleftharpoons H_2 + CO_2$, $\Delta H_{rxn,298K}$ = -41 kJ/mol H_2) results in the stoichiometric emissions of 5.5 kg CO_2/kg H_2, with the remaining emissions indirectly arising from steam generation and the high-grade heat required to sustain the SMR endothermic reaction and total up to ~12 kg CO_2/kg H_2. Oxidants play various roles in reforming processes. Steam provides half the hydrogen produced in SMR and is fed into the primary reforming reactor at mass ratios between 1.8-4 H_2O:CH_4(7). Incorporation of CO_2 in the feed (1 CO_2:CH_4) allows for dry reforming of methane (DRM) ($CH_4 + CO_2 \rightleftharpoons 2H_2 + 2CO$, $\Delta H_{rxn,298K}$ = 124 kJ/mol H_2), with stoichiometric emissions of 11 kg CO_2/kg H_2. Incorporation of oxygen in the feed (0.2-0.5 O_2:CH_4) allows for autothermal reforming (ATR) ($CH_4 + H_2O + ½\ O_2 \rightleftharpoons CO_2 + 3\ H_2$, $\Delta H_{rxn,298K}$ = -26 kJ/mol H_2) or partial oxidation ($CH_4 + ½\ O_2 \rightleftharpoons CO + 2H_2$, $\Delta H_{rxn,298K}$ = -19 kJ/mol H_2), which reduces the heat load but also increases the stoichiometric emissions (7.3 kg CO_2/kg H_2 and 11 kg CO_2/kg H_2, respectively)(7).

Non-oxidative conversion routes for methane have emerged as a new research opportunity for hydrocarbon utilization, including non-oxidative coupling(8), dehydroaromatization(9), and thermal decomposition or pyrolysis(10). Methane pyrolysis (MP) ($CH_4 \rightleftharpoons 2H_2 + C$, $\Delta H_{rxn,298K}$ = 37 kJ/mol H_2) has been proposed as a cost-competitive route to produce CO_2-free hydrogen with zero direct carbon emissions. During MP, methane decomposes in a non-oxidative environment to produce hydrogen and a solid carbon product that can either find value in the market or be sequestered in a much more stable and manageable form as compared to CO_2. MP plants can be located where H_2 is needed, the CH_4 feedstock can be provided using today's natural gas pipelines and solid-carbon product can be removed using today's truck or rail infrastructure. The fact that MP is compatible with today's infrastructure and does not need scaling of new types of infrastructure makes MP rapidly scalable and cost-effective, as long as the H_2 production costs are competitive in the H_2 market(11).

A key challenge for MP is the removal of the solid carbon from the reactor during the production of H_2. The efficient removal must be carefully managed to prevent pressure build-up

View Article Online
DOI: 10.1039/D5SC00768B

and catalyst loss. Several reactor configurations have been proposed to counter this challenge including fluidized bed reactors(12), moving bed reactors(13,14), molten media bubble columns(15), and plasma torch reactors(16). Sustaining high rates of methane conversion is also impeded by catalyst deactivation due to coke deposition.

This work aims to investigate whether a small, controlled amount of oxidant can prevent catalyst deactivation while maintaining the reducing environment necessary for the MP reaction to occur. To the best of our knowledge, oxidants during MP have only been used to supply in situ heat for the MP endothermic reaction at the expense of a decreased hydrogen and carbon yield(17). This approach, referred to as autothermal pyrolysis (ATP), is being commercialized by Ekona Power(18). Feeding oxygen to supply heat via combustion has also been explored across multiple pyrolysis-type processes not dealing with hydrogen production such as in-situ retorting for shale oil recovery(19), upgrading the heating value of low rank coals(20), and improving thermal degradation of biomass for biocrude and biochar production(21),[20,21].

Lastly, oxidants such as CO_2(22), H_2O(23,24), and O_2(25) have been demonstrated to enhance carbon nanotubes (CNTs) growth during chemical vapor deposition by mitigating catalyst sintering as well as selectively oxidizing amorphous carbon and annealing defects that would otherwise hinder CNTs growth. Unlike MP, chemical vapor deposition is solely optimized for CNTs growth. This focus on carbon inherently hinders its ability to also scale for hydrogen production due to expensive and dilute carbon feedstocks (typically 0.1-5 mol % of ethylene or acetylene), limited throughput to control kinetics, and low operating pressures to prevent undesired gas-phase reactions.

The addition of oxidants in MP is a seemingly counterintuitive strategy for a process theoretically designed to produce hydrogen with zero direct CO_2 emissions, which might explain why it has been scarcely investigated. However, potential environmental concerns related to oxidant use might be alleviated. For instance, the energy consumption of a Pressure Swing Adsorption (PSA) unit for hydrogen purification is minimal compared to the energy input required in conventional hydrogen production methods, such as SMR, where high-temperature heating constitutes a major operational cost(26). This work demonstrates the opportunity to complement MP with controlled amounts of oxidant co-feeds, shifting operation towards oxidant-assisted methane pyrolysis (OMP).

Previously, we described a semi-continuous process to produce H_2 and CNTs in a fluidized-bed reactor via repeated catalytic MP cycles that included in-situ carbon-catalyst separation steps(27). In this work, we demonstrate that the addition of a dilute oxidant, namely CO_2 or H_2O, in the reactor feed resulted in a net increase in carbon and hydrogen yields when compared against a pure methane feed. The increased extent of methane decomposition during OMP was associated to the in-situ cyclic phase change of the catalyst operated by the oxidant. The superior performance of OMP over conventional methane pyrolysis was demonstrated in two different reactor configurations, namely fluidized bed and monolithic reactor. In conclusion, this study introduces the route of OMP that, alongside ATP, completes the oxidative spectrum of methane utilization by bridging the gap between pyrolysis and reforming processes.

Results and discussion

Initial exploration of OMP was accomplished in a lab-scale fluidized bed reactor (FBR) operating at 750 °C with a 5 wt. % Fe/Al_2O_3 catalyst synthesized by wet impregnation of iron nitrate on 287 μm diameter alumina beads (**Figure 1A-B**). The objective was to monitor any

View Article Online
DOI: 10.1039/D5SC00768B

potential increase in methane conversion along with a corresponding rise in carbon and hydrogen yield. The in-situ reduced catalyst, exposed for 1 h to a flow of CH_4, displayed a total carbon yield of 2.43 ± 0.03 g_C/g_{Fe} and a hydrogen concentration in the effluent of ~1.4 vol. % at the end of the experiment (**Figure 1C-D**). The experiment was repeated by adding CO_2 (5 vol. %) as an oxidant to the gas feed mixture and resulted in a total carbon yield of 4.98 ± 0.20 g_C/g_{Fe} and a final hydrogen concentration in the effluent of ~11.9 vol. %. The simultaneous presence of CH_4 and CO_2 in a 95:5 volume ratio resulted in a twofold increase in carbon yield and a 7.5-fold increase in hydrogen concentration in the effluent when compared to the CH_4-only case.

A comparison of SEM images of the catalyst before and after reaction revealed thermomechanical stability of the alumina beads, which remained intact during pyrolysis, and the formation of a carbon layer on their surface (**Figure 1E-G**). When CO_2 was added to the feed, a thicker carbon layer was observed on the catalyst beads, confirming the net increase in carbon production (**Figure 1G**). Some of these thick carbon shells were found to peel off from the catalyst surface, likely because of mechanical abrasion under the fluidization regime (**Figure S1**).

View Article Online
DOI: 10.1039/D5SC00768B

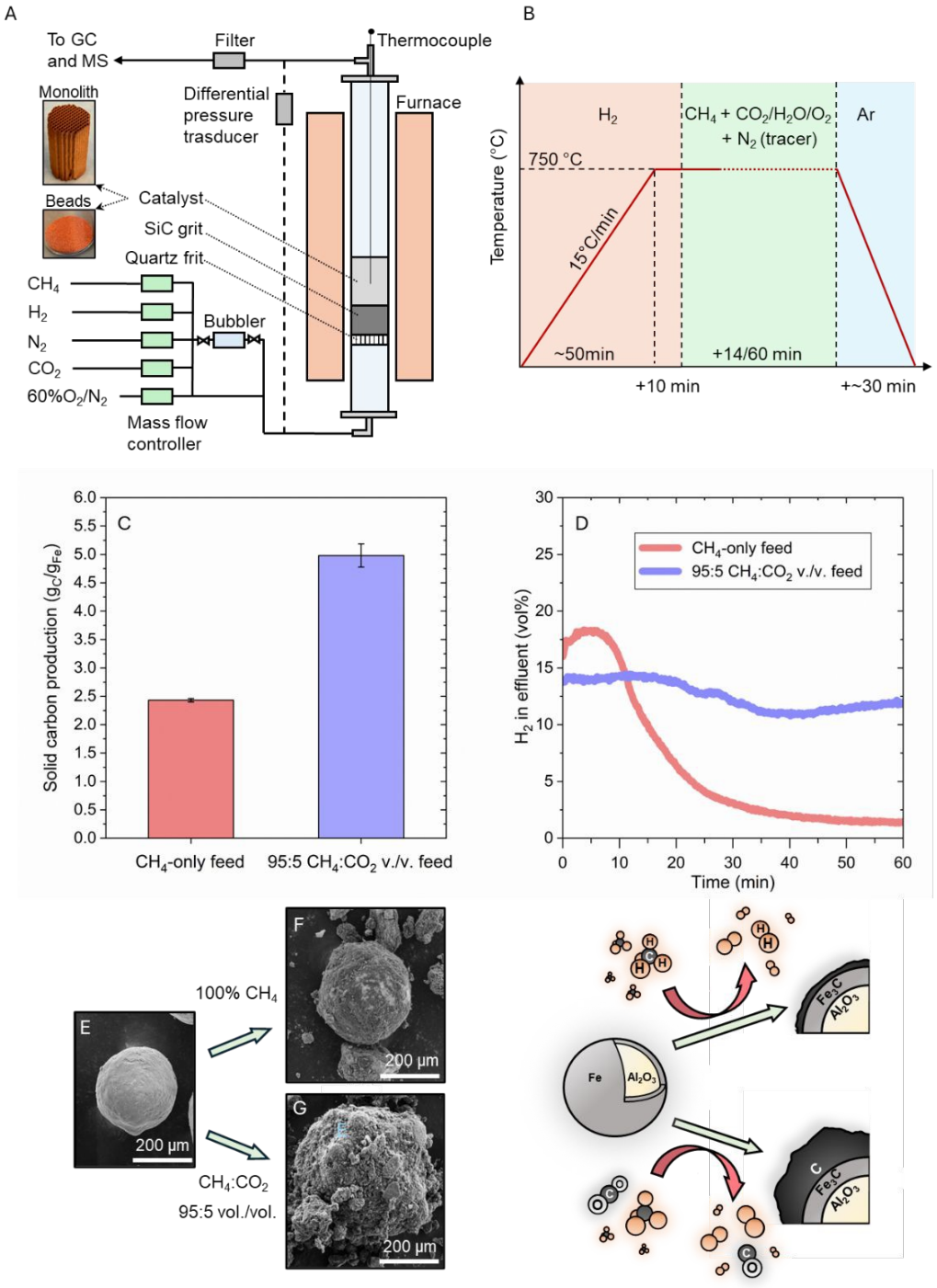

Figure 1. Comparison of methane pyrolysis (MP) and oxidant-assisted methane pyrolysis (OMP). **(A)** Schematic of the reactor set-up. **(B)** Graphical illustration of the reactor operation consisting of 3 steps: (i) heat-up + catalyst reduction, (ii) pyrolysis and (iii) cool-down under inert atmosphere. **(C)** Carbon yield, normalized by the Fe catalyst mass, and **(D)** hydrogen concentration in the effluent for CH_4-only and 95:5 CH_4:CO_2 vol./vol. reactor feed after 1 h at 750 °C (the maximum measurement uncertainty is ± 1.20% of the plotted values). **(E)** Catalyst bead before

View Article Online
DOI: 10.1039/D5SC00768B

reaction. **F)** Catalyst bead after reaction under CH_4 flow. **(G)** Catalyst bead after reaction under 95:5 CH_4:CO_2 vol./vol. flow. On the bottom right: graphical visualization of MP versus OMP.

We then explored whether other oxidants could lead to a similar increase in carbon yield under methane pyrolysis conditions. Selected oxidants, namely CO_2, H_2O, and O_2, were individually tested in the fluidized bed reactor by incrementally increasing their concentrations in the reactants stream at 750 °C. The percentage of solid carbon produced relative to the reference case of methane-only feed and the CO concentration in the reactor effluent, both measured after 14 min of reaction, were plotted against the methane-to-oxidant volume ratio (**Figure 2A-C**). The shorter duration of the experiment was used to ensure comparability in hydrodynamic conditions within the reactor as carbon was formed.

The methane-only experiment resulted in a carbon yield of 1.22 ± 0.01 g_C/g_{Fe} (corresponding to the [0%,0%] coordinate on the left y-axis of **Figure 2A-C**) and no detected CO in the effluent. The addition of incremental concentrations of CO_2 to the feed resulted in a monotonic increase in CO formation, while solid carbon production exhibited a maximum at 95:5 CH_4:CO_2 vol./vol. (**Figure 2A**). At this optimal gas feed composition, a carbon yield of 1.63 ± 0.03 g_C/g_{Fe} was measured, which corresponded to a 34% increase from the methane-only case. Beyond the 95:5 CH_4:CO_2 feed, the percentage of produced carbon showed a decline with increasing CO_2 fraction, eventually resulting in negative values that indicated lower carbon formation than the methane-only case. The appearance of a peak in carbon production supports the existence of an oxidant-assisted methane pyrolysis regime prior to the onset of dominant carbon gasification. The incremental addition of CO_2 in the methane feed was also tested with 5 wt. % Ni/Al_2O_3 and 5 wt. % Co/Al_2O_3 catalysts, which featured analogous behavior compared to the 5 wt. % Fe/Al_2O_3 catalyst (**Figure S2**).

Similar trends in solid carbon and CO production were observed when using H_2O as the oxidant. In this case, the maximum amount of carbon produced was found at a H_2O concentration in the reactor feed corresponding to 99.1:0.9 CH_4:H_2O vol./vol., which resulted in a carbon production of 1.60 ± 0.03 g_C/g_{Fe} – a 31% increase compared to the methane-only case (**Figure 2B**). As in the case of CO_2, the benefits gained from H_2O addition in low concentrations were negated at high concentrations due to lower carbon yield, likely resulting from higher rates of gasification of the carbon produced or from catalyst deactivation. CO concentration also increased with increasing H_2O concentrations, but at a slower rate compared to the CO_2 case.

Under increasing volume fractions of O_2 in the reactor feed, the carbon yield did not exhibit significant change compared to the methane-only case until 95.5:4.5 vol./vol. CH_4:O_2 (**Figure 2C**). Beyond this concentration, further O_2 addition resulted in decreasing amounts of collected solid carbon compared to the methane-only case. CO concentration in the effluent increased monotonically with O_2 co-feed fraction.

Across all experiments performed with an oxidant in the feed, CO_2 was not detected in the reactor effluent. Along with the CH_4 pyrolysis reaction (i.e. $CH_{4(g)} \rightarrow C_{(s)} + H_{2(g)}$), solid carbon can be produced through the CO disproportionation reaction (i.e. $2\ CO_{(g)} \rightleftharpoons C_{(s)} + CO_{2(g)}$), also known as the Boudouard reaction, which is thermodynamically viable, though not favored under the tested conditions (**Figure S3**). The lack of measurable CO_2 at the reactor outlet suggests that the Boudouard reaction did not contribute to the increase in solid carbon production observed.

In addition to the amount of carbon produced, the presence of an oxidant in the reactor could also affect the physical and chemical properties of the carbon. The investigated oxidants were previously shown to preferentially oxidize sp^3-hybridized carbon (defects in graphitic carbon or

View Article Online
DOI: 10.1039/D5SC00768B

amorphous carbon) over sp^2-hybridized carbon (graphitic carbon) and, at the same time, introduce defects on graphene lattices of graphite and CNTs(28–30). Raman spectroscopy was used to compare the degree of crystallinity of the various carbon samples, indicated by the ratio of the D ("defective" or "disordered", ~1350 cm^{-1}) and G ("graphitic", ~1580 cm^{-1}) peaks intensities. The G band is associated with graphene layers, while the D band with defects and, secondarily, to amorphous carbon.

The evolution of the I_D/I_G ratio at increasing oxidant-to-methane ratios in the reactor feed was measured for the individual cases of CO_2, H_2O, and O_2, respectively (**Figure 2D-F**). Carbon formed in presence of CO_2 featured an average I_D/I_G of 0.82 ± 0.11, very similar to the I_D/I_G of 0.90 ± 0.06 of the methane-only case. Carbon grown by the addition of H_2O in the feed featured an average I_D/I_G of 0.75 ± 0.08. Similarly, the carbon formed with O_2 in the feed featured an average I_G/I_D of 0.74 ± 0.06. Overall, the I_D/I_G of the various carbons fell within a narrow range, indicating comparable quality. The slightly reduced I_D/I_G values obtained by the addition of an oxidant suggested that, under the tested conditions, the presence of oxidants during carbon growth could reduce the formation of amorphous carbon and, possibly, not promote the formation of defects in the graphitic carbon.

Microscopy techniques were used to examine the morphology and microstructure of the carbon produced. Scanning electron microscopy (SEM) imaging mainly showed filamentous structures (**Figure 2G**), which featured similar range of length and diameter across all samples (**Figure S4**). Transmission electron microscopy (TEM) analysis revealed that the produced carbon exhibited a range of morphologies, primarily consisting of graphitic carbon, with a notable predominance of CNTs displaying a bamboo-like structure (**Figure 2H** and **Figure S5**). Iron nanoparticles were found to be encapsulated inside the CNTs, as evidenced by energy dispersive spectroscopy (EDS) analysis (**Figure S6**). Common across all oxidant co-feed cases, a significant amount of carbon was found on the reactor walls, a phenomenon that was not observed in the methane-only feed (**Figure S7**). The facile separation of carbon from the catalyst surface in the form of carbon shells (**Figure S1**) demonstrated the opportunity for a more straightforward carbon removal from the reactor.

View Article Online
DOI: 10.1039/D5SC00768B

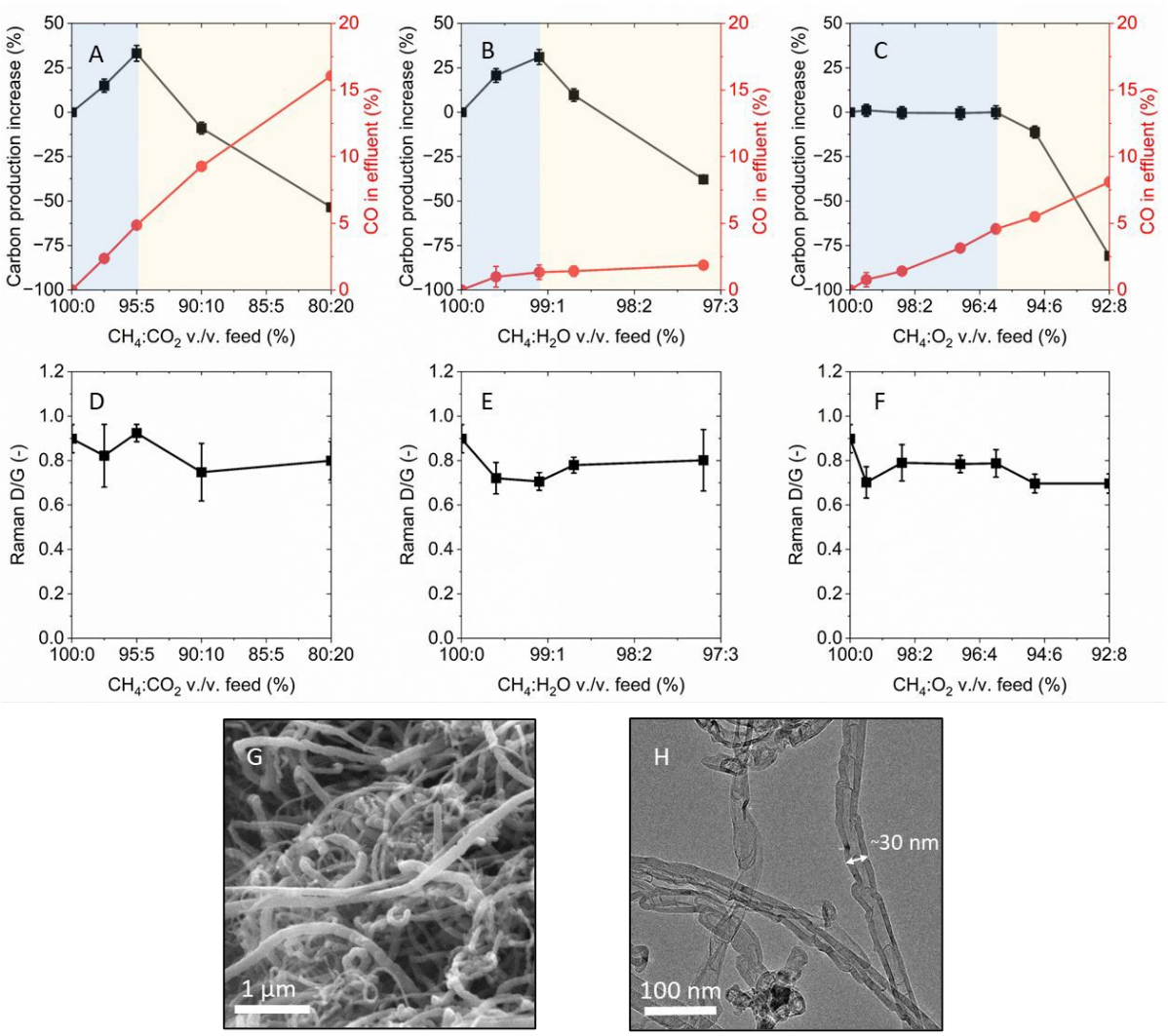

Figure 2. Product yield and carbon quality for different OMP conditions. Percentage of carbon produced relative to the methane-only feed experiment (left y-axis) and CO concentration in the reactor effluent (right y-axis) as a function of methane-to-oxidant vol./vol. ratio in the feed for (**A**) CO_2, (**B**) H_2O and (**C**) O_2. On each plot, the area highlighted in blue indicates the OMP-controlled regime, while the area highlighted in yellow denotes the gasification-controlled regime. Raman I_D/I_G as function of methane-to-oxidant vol./vol. ratio for (**D**) CO_2, (**E**) H_2O and (**F**) O_2. SEM (**G**) and TEM (**H**) images of the carbon produced with a CH_4-only feed.

The increase in solid carbon yield observed with the addition of CO_2 and H_2O in low concentrations was lost at higher concentrations (**Figure 2A-B**). Ex-situ X-Ray Diffraction (XRD) analysis of the spent catalysts of the CO_2 co-feed case provided insights into the potential mechanism behind the observed change in activity at increasing oxidant concentration (**Figure 3A**). A consistent trend was observed across the H_2O and O_2 co-feeds cases as well (**Figure S8-9**). Cementite (Fe_3C) peaks at 43.7°, 45.1°, 48.6°, and 49.0° were the only distinguishable iron phase peaks present for the methane-only feed, as well as every oxidant co-feed which resulted in

View Article Online
DOI: 10.1039/D5SC00768B

a net positive increase in solid carbon production. At oxidant concentrations associated with a decrease in solid carbon production, namely 80:20 CH_4:CO_2 vol./vol. (**Figure 3A**), the cementite phase peaks were lost and replaced by a combination of metallic iron (peaks 44.7°, 65.0°, and 82.3°) and magnetite (Fe_3O_4, peaks 30.5° and 36.5°). Cementite phase loss was also observed for both the 97.2:2.8 CH_4:H_2O vol./vol. and 92:8 CH_4:O_2 vol./vol. feed samples, which resulted in mixtures of magnetite, wüstite (FeO), and reduced metallic iron (**Figure S8-9**).

Iron shows two stable crystal structures depending on temperature: the face-centered cubic (FCC) austenite (γ-iron) phase and the body-centered cubic (BCC) ferrite (α-iron) phase. The conditions used in this work were above the threshold temperature for α-to-γ Fe phase transition (723°C for >0.02wt% C), and austenite was expected to be the thermodynamically stable state of iron. Its FCC structure allows for higher carbon solubility and the formation of carbide species(31). Cementite is frequently reported as the active catalyst phase during methane decomposition(32–34), though some studies suggest metallic iron is more active than cementite near our operating temperature(35). Regardless of cementite activity, it is an ensuing intermediate phase of methane decomposition as iron is a carbide-forming metal and any fully dehydrogenated carbon atoms chemisorbed on its surface will diffuse into the catalyst bulk(36). The presence of oxidized catalyst phases at higher oxidant co-feed concentrations may explain the observed loss of activity. This also suggests that catalyst oxidation may be occurring to some degree at the lower oxidant concentrations leading to an increase in solid carbon production, potentially shedding light on the mechanism of OMP.

To investigate in more detail the interactions between the oxidant and the surface of the catalyst that led to increased carbon production, the methane and oxidant feeds were separated into two consecutive stages to probe their individual effects on the catalyst phase and composition. Pyrolysis with pure methane was performed for 10 min at 750 °C to produce cementite phase and carbon. The reactor was then purged with argon to remove hydrogen and unreacted methane. The optimized 95:5 CH_4:CO_2 vol./vol. feed was then introduced into the reactor at the same flow rates employed during OMP operation but using argon instead of methane while tracking effluent concentration (**Figure 3B**). The only relevant species leaving the reactor were CO and CO_2 at concentrations that indicated a CO_2 conversion of approximately 93%. This conversion exceeded the thermodynamic limit of 64% expected if CO_2 reacted solely with the carbon product via the reverse Boudouard reaction (**Figure S3**), indicating that the CO_2 must also have reacted with the catalyst.

To further investigate the role of catalyst reactivity with CO_2, a pure cementite catalyst phase without carbon was successfully produced by treating the catalyst under a pure methane feed at 500 °C for 1 h prior to reaction following a previous published work (**Figure S10**)(37). Ex-situ XRD demonstrated that this produced cementite phase was stable even after 30 min at 750°C under argon, as well as after exposure to ambient air during transport to the XRD instrument. The experiment outlined previously using 95:5 Ar:CO_2 vol./vol was then replicated using this pure cementite catalyst phase. Sustained CO_2 conversion into CO was observed for ~10 min before declining until a complete loss of CO detection occurred at ~20 min (**Figure 3C**). Ex-situ XRD revealed that the cementite phase was completely converted into magnetite and wüstite phases after reaction with CO_2 (**Figure S11**).

The initial effluent concentration was comparable between the experiments starting with either cementite and carbon (**Figure 3B**) or only cementite (**Figure 3C**). This result suggested that CO_2 mostly reacted with the cementite phase as opposed to reacting with carbon in the reverse

View Article Online
DOI: 10.1039/D5SC00768B

Boudouard reaction and the sustained activity in **Figure 3B** was due to the presence of excess carbon capable of regenerating the cementite phase. The presence of iron oxide species on the spent catalyst from **Figure 3C** indicated that CO_2 oxidized metallic iron without the presence of either carbon or methane to regenerate the lost cementite phase (**Figure S11**).

The experiments above were reproduced using the optimized 99.1:0.9 CH_4:H_2O vol./vol. feed to also understand the interaction between the H_2O co-feed and the catalyst surface. The reactor effluent from a catalyst initially containing both cementite and free carbon was tracked (**Figure 3D**), as well as the reactor effluent using a pure cementite phase catalyst (**Figure 3E**). Interestingly, the only product observed in both experiments was hydrogen, with no detection of CO. Unlike the CO_2 co-feed, which can only produce CO in all its reactions with cementite, carbon, and metallic iron, the product distribution observed under a H_2O co-feed is highly dependent on which reaction it participates in. The lack of measurable CO_x in the reactor effluent indicated that H_2O could not have reacted with any carbonaceous species, but instead only reacted with the iron in the cementite phase. This observation also suggested that the CO evolution observed during OMP with the 99.1:0.9 CH_4:H_2O vol./vol. feed (**Figure 2B**) must have resulted from methane acting as the reductant for the iron oxide produced in-situ (**Figure S12**).

Given that in both the 95:5 CH_4:CO_2 vol./vol. and 99.1:0.9 CH_4:H_2O vol./vol. feed the oxidants readily reacted with cementite, and that cementite was the only iron phase detected on the spent catalysts (**Figure 3A** and **Figure S8**), we conclude that cyclic formation-decomposition of cementite was occurring in-situ and explained the increase in carbon production during OMP. As a metastable species at 750 °C, there exists a thermodynamic driving force for cementite to either undergo a reaction or decompose into a more stable state of austenite and graphite. The limited stability of cementite is contingent on the highly reducing methane atmosphere and the source of carbon imparted by methane decomposition. While carbon gasification and dry reforming rates over Fe catalysts are sufficiently low at 750 °C(38,39), small concentrations of mild oxidants like CO_2 and H_2O may be able to selectivity oxidize cementite due to its inherent instability at this temperature.

The oxidation of either iron or carbon in the cementite lattice shifts the phase equilibria, which may accelerate cementite decomposition as its stability is highly dependent on the local concentrations of iron and carbon(40). The decomposition of cementite into austenite and graphite results in a material volume expansion of 13.8%(40), which may be capable of delaminating the carbon shells encapsulating the catalyst. This hypothesis may explain the significant amounts of dislodged carbon found in the catalyst bed and lining the reactor walls after the reaction.

In summary, the enhanced methane conversion observed under the CO_2 and H_2O co-feeds may be explained by two different processes (**Figure 3F**). On one side, the dislodgement of carbon from the catalyst surface occurs because of phase change that regenerated the active sites. On the other side, metallic iron formed from the decomposition of cementite may be a more active catalyst for methane decomposition and the mild oxidants helped suppress cementite formation(35). These processes may be occurring synergistically.

View Article Online
DOI: 10.1039/D5SC00768B

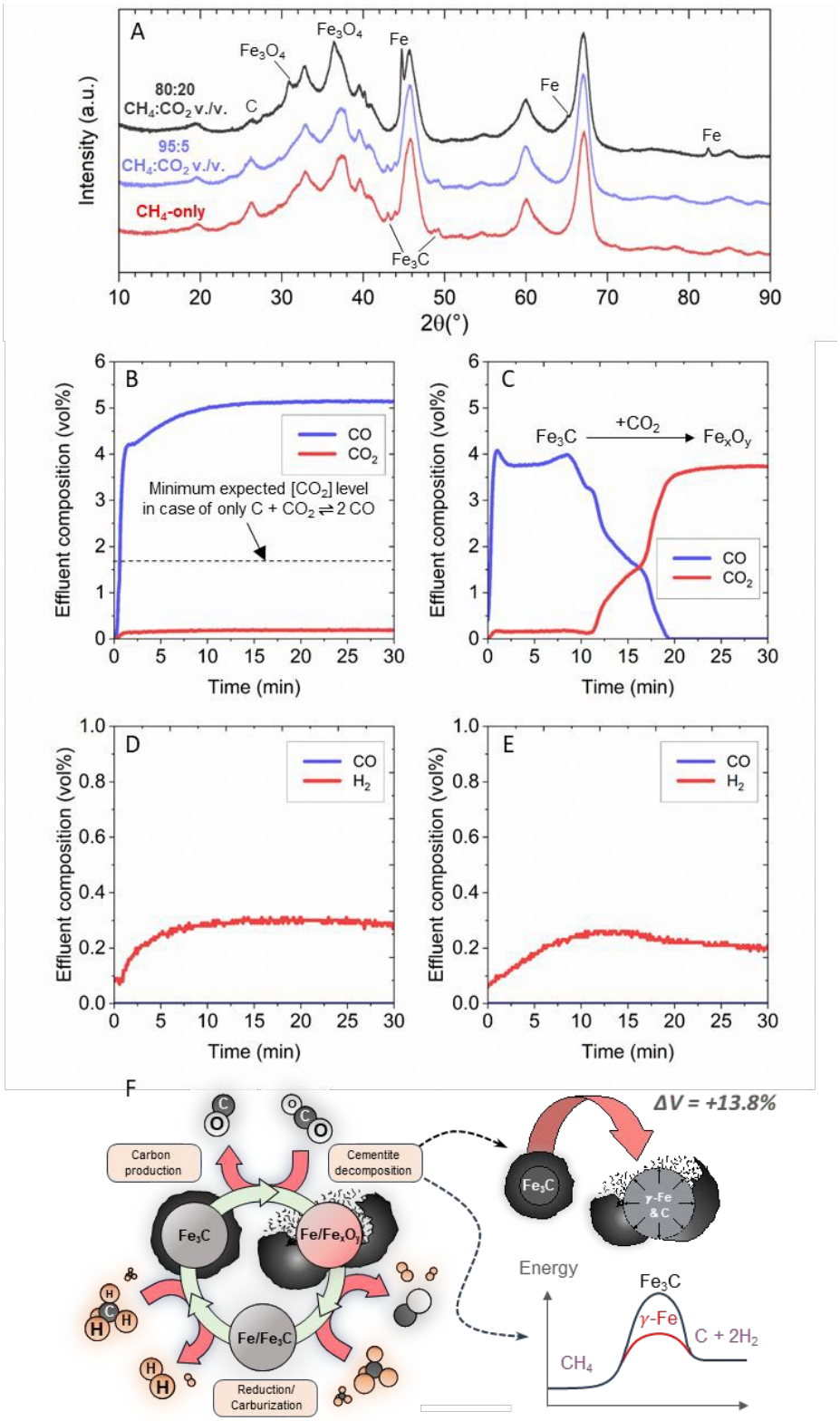

Figure 3. Mechanism for the enhanced catalytic activity in OMP. (**A**) XRD spectra of 5 wt% Fe/θ-Al_2O_3 catalysts tested under methane-only, 95:5 CH_4:CO_2 vol./vol. and 80:20 CH_4:CO_2 vol./vol. feed. (**B**) Fe_3C and C mixture tested under a 95:5 Ar:CO_2 vol./vol. feed (**C**) Fe_3C tested under a

View Article Online
DOI: 10.1039/D5SC00768B

95:5 Ar:CO_2 vol./vol. feed. (**D**) Fe_3C and C mixture tested under a 99.1:0.9 Ar:H_2O vol./vol. (**E**) Fe_3C tested under a 99.1:0.9 Ar:H_2O vol./vol. feed. (**F**) Graphical visualization of in-situ cyclic formation-decomposition of cementite.

To gauge the overall performance of CO_2 and H_2O co-feeds at their optimal concentrations, methane conversion in the FBR was tracked for each condition with a weight hourly space velocity (WHSV) of ~14.5 hr^{-1} and compared against a methane-only feed (**Figure 4A**). Oxygen was not included because it introduced emissions without increasing solid carbon production. All three experiments started with a methane conversion of ~30% followed by a decline and stabilization at a pseudo-steady state conversion. Methane conversion for the 95:5 CH_4:CO_2 vol./vol. feed performed the best with a steady-state conversion at 1 h of 18.1%, followed by 2.8% for the 99.1:0.9 CH_4:H_2O vol./vol. feed and 1.5% for the methane-only feed. This trend in methane conversion also correlated with solid carbon production of 4.98 ± 0.20 g C/g Fe, 2.89 ± 0.25 g C/g Fe, and 2.43 ± 0.03 g C/g Fe, respectively.

As was commonly observed across all OMP experiments, both the 95:5 CH_4:CO_2 and 99.1:0.9 CH_4:H_2O vol./vol. feeds featured substantial accumulations of carbon within the bed and along the reactor walls, whose dislodgement from the catalyst surface was likely aided by fluidization-induced abrasion. Fluidized catalytic cracking units also suffer from attrition(41), making it reasonable to assume that it provides a means for carbon separation and removal with a cost-effective catalyst. As gas-solid separation and removal was not the focus of this work, the produced carbon was allowed to accumulate in the bed during operation.

The discrepancy in methane conversion observed between the 95:5 CH_4:CO_2 and 99.1:0.9 CH_4:H_2O vol./vol. feed may be explained by the different hydrodynamics each system experienced during operation. It is well known that the hydrodynamics and performance of a fluidized bed reactor are highly dependent on many parameters that are inherently dynamic in methane pyrolysis. Specifically, the solid carbon production that results from methane decomposition changes the diameter, density, and sphericity of the fluidized particle, all of which directly affect fluidization with a compounding effect on performance(42).

Additionally, the CO_2 co-feed conditions resulted in the emission of almost four times more CO than the H_2O co-feed (**Figure 2A-B**). This increase in CO production must ultimately result from the consumption of methane feedstock, which means that the CO_2 co-feed did not produce as much net solid carbon as an H_2O co-feed for the same methane conversion. The higher initial rate of carbon deposition under the 99.1:0.9 CH_4:H_2O vol./vol. feed meant that the two systems experienced different rates of changes to their hydrodynamics. This observation may partially explain why methane conversion under the 99.1:0.9 CH_4:H_2O vol./vol. feed was lower than that of the 95:5 CH_4:CO_2 vol./vol. feed (**Figure 4A**).

To avoid the influence of hydrodynamics on methane decomposition as well as assess how effectively OMP could be translated to other reactor configurations, the process was tested in a monolithic reactor configuration with the same WHSV of ~14.5 hr^{-1} as the FBR. The monolithic reactor helped reduce pressure drop across the bed and increased heat and mass transfer rates. This design was particularly advantageous for methane decomposition processes compared to traditional packed bed reactors as its larger open area allowed for more carbon accumulation before clogging and pressure build-up events.

The main benefit of using the monolithic reactor in this study was to fairly compare the two oxidant co-feeds under similar hydrodynamic environments. Using Fe/Al_2O_3 catalyst wash-coated on the monolithic cordierite substrate, an initial methane conversion greater than 65% was

View Article Online
DOI: 10.1039/D5SC00768B

observed for both the 95:5 CH_4:CO_2 and 99.1:0.9 CH_4:H_2O vol./vol. feeds (**Figure 4B**). The quality of the carbon formed in the monolithic reactor was comparable to that from the FBR (**Figure S13**). The 99.1:0.9 CH_4:H_2O vol./vol. feed accumulated carbon at a higher rate than the other two conditions, which led to clogging and an ensuing pressure increase which required the experiment to be stopped at an earlier time. The pure methane feed also started at the same initial methane conversion, but slowly decreased to ~35% by the end of the experiment demonstrating that OMP outperformed MP in both the FBR and monolithic reactor.

The experimental data from the monolithic reactor were utilized to assess the potential economic advantages of integrating OMP processes into a gas turbine power plant. A preliminary technoeconomic analysis (TEA) of this case study suggested that the OMP-integrated process could result in lower electricity costs compared to the integration of conventional MP or direct methane combustion, mainly due to the additional revenue from selling the co-produced solid carbon (details of the TEA are presented in the Supplementary Information). This application of OMP exemplifies the potential of this approach in advancing the clean energy transition. Pipeline-quality natural gas typically contains up to ~4 vol% CO_2 and water vapor concentrations up to ~0.17 vol%(43,44). These values correspond with the lower end of the beneficial oxidant concentrations reported in this study. This alignment suggests that the oxidant-assisted methane pyrolysis approach presented here could be implemented directly with natural gas streams, without the need of pre-treatment. Furthermore, the process may offer a route to valorize natural gas resources with higher oxidant content that are currently underutilized due to processing costs and emissions constraints.

View Article Online
DOI: 10.1039/D5SC00768B

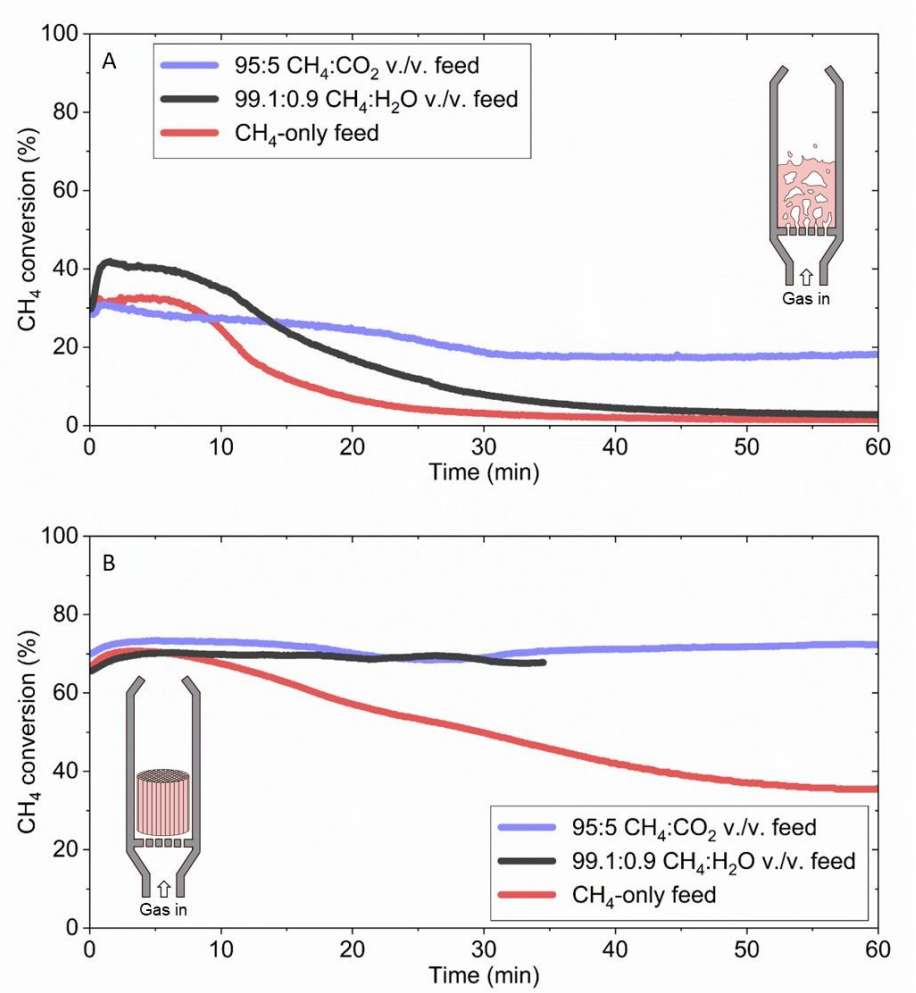

Figure 4. Comparison of OMP versus MP performance in different reactor configurations. Methane conversion as function of time in (**A**) fluidized-bed and (**B**) monolithic reactor. The maximum measurement uncertainty is ± 1.20% of the plotted values for both the CH_4-only and 95:5 CH_4:CO_2 vol./vol. feeds in both reactor configurations, while for the 99.1:0.9 CH_4:H_2O vol./vol. feed it is ± 6.36% of the plotted values in the FBR, and ± 1.40% of the plotted values in the monolithic reactor.

Conclusions

In this study, the concept of oxidant-assisted methane pyrolysis (OMP) was introduced. At first, it was demonstrated that the addition of a small amount of CO_2 to a methane feed entering a fluidized bed of Fe/Al_2O_3 catalyst at 750 °C resulted in a two-fold increase in carbon yield compared to methane-only feed over 1 h operation, with a corresponding increase in hydrogen yield and producing CO as a side product. The presence of CO_2 enabled the formation of a thick carbon layer on the catalyst beads prone to detachment under fluidization-induced abrasion. The introduction of other oxidants, such as H_2O and O_2, was also investigated. Optimal oxidant-to-methane ratios for carbon formation were identified for both CO_2 and H_2O, beyond which gasification became dominant. Peak carbon yields were measured for 95:5 CH_4:CO_2 vol./vol. and

View Article Online
DOI: 10.1039/D5SC00768B

99.1:0.9 CH_4:H_2O vol./vol. feeds, which resulted in a carbon production increase of 34% and 31%, respectively, compared to the methane-only feed over 14 min operation. Similar results were also observed for Ni/Al_2O_3 and Co/Al_2O_3 catalysts tested with a CO_2 co-feed under the same conditions. Raman spectroscopy indicated that oxidant addition slightly promoted the removal of amorphous carbon, enhancing the accumulation of graphitic carbon in the product. Microscopy techniques revealed the predominant formation of carbon nanotubes (CNTs) across all conditions.

Cementite (Fe_3C) was identified as a crucial intermediate for methane decomposition, with experiments evidencing its cyclic formation and decomposition when CO_2 and H_2O were introduced. The decomposition of cementite, accelerated by the oxidant, enhances the production of carbon by facilitating the regeneration of active sites on the catalyst surface. These findings reveal a dynamic process in which catalyst phases are continually evolving. At high oxidant concentrations, the transition from cementite to iron oxides accounts for the observed decline in catalyst activity and highlights the importance of optimizing oxidant levels for the effective operation of methane pyrolysis.

Comparative studies in both fluidized bed and monolithic reactor configurations confirmed that methane conversion rates and solid carbon accumulation were higher under CO_2 and H_2O co-feeds compared to the methane-only feed, validating the effectiveness of OMP across different reactor types.

Overall, this study highlights the potential of oxidant-assisted methane pyrolysis as an innovative approach to enhance catalyst performance and product yields relative to conventional methane pyrolysis, paving the way for more efficient production of hydrogen and crystalline carbon.

Methods

Catalysts preparation

The catalyst beads used in the fluidized bed reactor configuration were prepared using 287 μm avg. diameter beads made of θ-Al_2O_3 (Puralox 300/130 from Sasol), sieved to remove the fraction below 250 μm. $Fe(NO_3)_3 \cdot 9H_2O$ (99+%, for analysis from Thermo Fisher Scientific) was dissolved in deionized water and the resulting solution was added dropwise to the Al_2O_3 beads, shaken by a vortex mixer, to obtain a 5 wt% Fe loading on the total final catalyst mass. The slurry was dried for approx. 2 h in a rotary evaporator (60 °C at 20 rpm and 20 mbar) then calcined in air at 450 °C for 5 h, with heating and cooling at 2 °C/min. After calcination, the catalyst was sieved to remove residual loose powder and stored in a vacuum desiccator until usage. The catalyst was reduced in-situ by heating up to 750 °C at 15 °C/min under a 500 sccm H_2 flow and holding at those conditions for 10 min. Some experiments required Fe_3C as the initial catalyst phase, which was prepared in-situ following the procedure described by Pilipenko et al(37). As-synthesized catalyst was reduced under H_2 at 750 °C then cooled down to 500 °C, where it was isothermally carburized for 1 h under a 285 sccm CH_4 flow. Afterwards, the system was brought back to the reaction temperature of 750 °C under Ar. XRD analysis confirmed the presence of Fe_3C and the absence of free carbon both at the end of in-situ carburization and after 30 min at 750 °C under Ar, which proved that Fe_3C does not thermally decompose (**Figure S10**).

View Article Online
DOI: 10.1039/D5SC00768B

Monolithic catalysts were prepared from a cordierite honeycomb substrate (400 cspi from Corning). The original 6x6" monolith substrate was cut with a hole saw to obtain 0.75"-dia. cylindrical pieces of ~1.5" length. The substrate pieces were dried for 2 h in a vacuum drying oven (80 °C at -25 inHg) and then coated with a porous layer of Al_2O_3 (**Figure S14**). For the coating, a slurry was prepared by mixing 20 wt% of Al_2O_3 powder (Puralox SCFa140 UF3 from Sasol, with a 138 m^2/g SSA) jet-milled down to an average particle diameter of 3.5 µm, with 5 wt% of uncalcined bohemite binder (Disperal P2 from Sasol) and 75 wt% of deionized water. The slurry was vigorously shaken for 10 min, then its pH adjusted to 3.5 with the addition of acetic acid (glacial, from Fisher Chemical), and finally shaken again for 10 min. The monolith substrates were submerged into the slurry for 1 min, then passed under a sheet of high-velocity dry air created with an air knife (air pressure set at 70 psi). The passes were alternated on both sides until all excess slurry was blown away and a thin layer was left. The slurry-coated monoliths were dried for 2 h in a vacuum drying oven (80 °C at -25 inHg), then calcined in air at 870 °C for 4 h with 2 °C/min as heating and cooling ramp. The Al_2O_3 coating procedure (submersion in slurry, removal of excess slurry, drying and calcination) was performed once again to deposit another layer of porous Al_2O_3 before the Fe catalyst loading. Al_2O_3-coated monoliths were submerged into a 1 M solution of $Fe(NO_3)_3 \cdot 9H_2O$ in deionized water for 30 min, then passed under a sheet of high-velocity dry air (air pressure set at 40 psi), alternating both sides, to remove excess solution. The nitrate-solution-loaded monoliths were dried for 2 h in a vacuum drying oven (80 °C at -25 inHg), then calcined in air at 450 °C for 5 h with 2 °C/min as heating and cooling ramp. The Fe loading procedure (submersion in nitrate solution, removal of excess solution, drying and calcination) was repeated 5 times to load ~7-8 wt.% Fe on the total catalyst mass.

Reactor setup and performance

Pyrolysis experiments were carried out in a bench-scale reactor set-up, customizable for either fluidized or monolithic bed configuration. A fritted, 20-mm-ID, 25-mm-OD, quartz tube (from Prism Research Glass) was vertically positioned in an electrical furnace with a 440-mm-long heating zone (from MTI Corp). A 5-cm-long bed of SiC grit (from Kramer Industries) was used to pre-heat and distribute the gas entering the reactive zone. In the fluidized bed configuration, the reactive bed consisted of 5 wt% Fe/θ-Al_2O_3 catalyst. 14.3 g of as-produced catalyst beads were used for the 14-min-long experiments, while 17.0 g for the 1-h-long ones. In the monolith bed configuration, two 0.75"-diameter, 1.5"-long Al_2O_3-coated monoliths with a ~7-8 wt.% Fe loading and total weight of ~5g were placed on top of each other. A K-type thermocouple (from Omega Engineering, Inc.) was placed right at the top of the reactive zone to monitor its temperature, while a differential pressure transducer (from Omega Engineering, Inc.) was used to measure the pressure across the reactor. Mass flow controllers (model DPC17 from Aalborg) were used to flow the gases (99.999%, from Airgas). The desired amount of H_2O was introduced in the reactor by flowing the appropriate amount of dry gas through a glass bubbler filled with deionized water at ambient temperature. The water saturation level of the gas was measured with off-line measurements using a humidity sensor (HMT120 from Vaisala) and was typically ~80%. The gas exiting the reactor was filtered with a 2-µm-pore-size paper filter (from Savillex Corp.) before being sampled by a mass spectrometer (HPR-20 R&D from Hiden Analytical), and a gas chromatographer (from SRI Instruments) equipped with both a thermal conductivity detector and flame ionization detector with a methanizer. In a typical run, the reactor was heated up to 750°C at 15°C/min under a 500 sccm H_2 flow and held at those conditions for 10 min to reduce the

View Article Online
DOI: 10.1039/D5SC00768B

catalyst. Next, in the case of fluidized bed configuration, a 285 sccm CH_4 flow was supplied together with the appropriate flow of oxidizer (CO_2, H_2O or O_2) to give the desired feed composition for pyrolysis. The flowrates during both reduction and pyrolysis were chosen to be approximately twice the minimum fluidization velocity measured for each gas. A N_2 flow was also fed to the reactor to serve as an inert tracer for gas composition analysis. 50 sccm N_2 were used for the 14-min-long experiments and 110 sccm N_2 for the 1-h-long ones. In the case of monolithic bed configuration, the only difference consisted in the value of CH_4 and oxidizer flow rates, which were adjusted to match the same weight hourly space velocity (WHSV, calculated as mass flow rate of CH_4 divided the mass of Fe) of the 1-h-long experiments in the fluidized-bed reactor configuration. A CH_4 flow between 120 and 130 sccm (adjusted within this range depending on the monolith weight) was supplied together with the appropriate flow of oxidizer (CO_2, H_2O or O_2) to give the desired feed composition. After the reaction stage, a 200 sccm Ar flow was supplied to prevent further reactions while cooling down to room temperature. After the experiment, the mixture of catalyst and produced carbon was separated from the SiC grit by sieving. The CH_4 conversion was calculated as

$$X = \frac{\dot{n}_{\mathrm{CH_4,\,in}} - \dot{n}_{\mathrm{CH_4,\,out}}}{\dot{n}_{\mathrm{CH_4,\,in}}}$$

where $\dot{n}_{\mathrm{CH_4,\,in}}$ and $\dot{n}_{\mathrm{CH_4,\,out}}$ are the inlet and outlet CH_4 molar flow rates, respectively. While the first is a known value, the second was calculated by comparing the measured outlet concentration against a calibration curve, which was derived with concentrations measured while flowing the same N_2 flow rate as in the experiments.

Materials characterization

The catalyst and the produced carbon were characterized with a series of analytical techniques. X-ray diffraction (XRD) analysis was performed with a Rigaku MiniFlex 600 X-ray diffractometer using a copper K-α radiation source (λ= 1.5405 Å) operated at 40 kV and 15 mA. Scanning electron microscopy (SEM) images were obtained using a Thermo Fisher Scientific Apreo S LoVac microscope, with detection of both secondary and backscattered electrons. Raman spectroscopy was performed using a HORIBA Scientific XploRA+ Confocal Raman spectrometer with a 532-nm laser source. Transmission Electron Microscopy (TEM) images were collected with a Thermo Fisher Scientific Spectra 300 transmission electron microscope with a field-emission gun operating with an accelerating voltage of 300 kV. A SuperX energy dispersive spectroscopy (EDS) detector integrated in the transmission electron microscope was used to perform elemental analysis. Thermodynamic data were derived using the FactSage 8.3 database.

Author contributions

M. G., H. M., V. H., A. T., J. P. S., E. S., R. G., A. M. and M. C. designed the project. M. G., H. M., J. F., A. N. and H. V. synthesized the catalyst. M. G. and H. M. performed the pyrolysis experiments and characterizations. M. G., D. S. and A. B. conducted the technoeconomic analysis. A. M. and M. C. supervised the project. M. G. and H. M. wrote the manuscript, with input and revisions by all authors.

View Article Online
DOI: 10.1039/D5SC00768B

Declaration of interests

A provisional patent with the findings reported in this work was filed by Susteon Inc. and Stanford University.

Data availability

The authors declare that the data supporting the findings of this study are available within the article and the ESI.

Acknowledgments

The information, data, or work presented herein was funded by the Advanced Research Projects Agency-Energy (ARPA-E), U.S. Department of Energy, under award no. DE-AR0001192 - SPO 159211. Additional funding was provided by the CO_2 Research Center (CORC), supported by the Novo Nordisk Foundation, to M.G., and the Stanford University Natural Gas Initiative to H.M. Part of this work was performed at the Stanford Nano Shared Facilities (SNSF), supported by the National Science Foundation under award ECCS-2026822. We thank Marcos Schöneborn of Sasol Inc. for providing us with the catalyst precursors; and Scott Barton of the Stanford Physics Store and Mehmet Solyali of the Stanford Machine Shop for assisting with the procurement and adaptation of reactor parts.

References

1. bp Energy Outlook 2024. Available from: https://www.bp.com/en/global/corporate/energy-economics/energy-outlook.html.
2. Sarpong KA, Xu W, Gyamfi BA, Ofori EK. A step towards carbon neutrality in E7: The role of environmental taxes, structural change, and green energy. *J Environ Manage*. 2023; 337:117556.
3. Rojas J, Zhai S, Sun E, Haribal V, Marin-Quiros S, Sarkar A, et al. Technoeconomics and carbon footprint of hydrogen production. *Int J Hydrogen Energy*. 2024; 49:59–74.
4. International Energy Agency (IEA). Global Hydrogen Review 2023. 2023 Available from: https://www.iea.org/reports/global-hydrogen-review-2023
5. Hydrogen Shot | Department of Energy. Available from: https://www.energy.gov/eere/fuelcells/hydrogen-shot
6. Cho HH, Strezov V, Evans TJ. Environmental impact assessment of hydrogen production via steam methane reforming based on emissions data. *Energy Reports*. 2022; 8:13585–95.
7. Bartholomew CH, Farrauto RJ. Fundamentals of industrial catalytic processes. 2006; 966.
8. Wang J, Rao Z, Huang Z, Chen Y, Wang F, Zhou Y. Recent Progress of Metal-Oxide-Based Catalysts for Non-Oxidative Coupling of Methane to Ethane and Hydrogen. *Catalysts*. 2023; 13(4):719.
9. Menon U, Rahman M, Khatib SJ. A critical literature review of the advances in methane dehydroaromatization over multifunctional metal-promoted zeolite catalysts. *Appl Catal A Gen*. 2020; 608:117870.

View Article Online
DOI: 10.1039/D5SC00768B

10. Sánchez-Bastardo N, Schlögl R, Ruland H. Methane Pyrolysis for Zero-Emission Hydrogen Production: A Potential Bridge Technology from Fossil Fuels to a Renewable and Sustainable Hydrogen Economy. *Ind Eng Chem Res*. 2021; 60(32):11855–81.
11. Sun E, Sarkar A, Gigantino M, Randall R, Jaffer S, Rojas J, et al. Requirements for CO_2-free hydrogen production at scale. *Joule*. 2024; 8(6):1539–43.
12. Dunker AM, Kumar S, Mulawa PA. Production of hydrogen by thermal decomposition of methane in a fluidized-bed reactor—Effects of catalyst, temperature, and residence time. *Int J Hydrogen Energy*. 2006; 31(4):473–84.
13. Maass HJ, Goeke V, Machhammer O, Guzmann M, Schneider C, Hormuth WA, Bode A, Klingler D, Kern M, Kolios G, inventors; BASF SE, assignee. Method for the parallel production of hydrogen and carbon-containing products. United States patent US 9,359,200. 2016 Jun 7.
14. Pohlenz JB, Scott NH, inventors; Universal Oil Products Co, assignee. Method for hydrogen production by catalytic decomposition of a gaseous hydrocarbon stream. United States patent US 3,284,161. 1966 Nov 8.
15. Upham DC, Agarwal V, Khechfe A, Snodgrass ZR, Gordon MJ, Metiu H, McFarland EW. Catalytic molten metals for the direct conversion of methane to hydrogen and separable carbon. *Science*. 2017; 358(6365):917–21.
16. Gautier M, Rohani V, Fulcheri L. Direct decarbonization of methane by thermal plasma for the production of hydrogen and high value-added carbon black. *Int J Hydrogen Energy*. 2017; 42(47):28140–56.
17. Muradov N, Smith F, Huang C, T-Raissi A. Autothermal catalytic pyrolysis of methane as a new route to hydrogen production with reduced CO_2 emissions. *Catal Today*. 2006; 116(3):281–8.
18. Alhamed H, Behar O, Saxena S, Angikath F, Nagaraja S, Yousry A, Das R, Altmann T, Dally B, Sarathy SM. From methane to hydrogen: A comprehensive review to assess the efficiency and potential of turquoise hydrogen technologies. *Int J Hydrogen Energy*. 2024; 68:635–62.
19. Xu S, Sun Y, Guo W, Yang Q, Li Q, Guo M, et al. Regulating the oxidative assisted pyrolysis of Huadian oil shale by preheating temperature and oxygen flow rate. *Energy*. 2023; 262:125602.
20. Qi J, Fan C, Li S. Characteristics of lignite char derived from oxy-pyrolysis. *Fuel*. 2021; 291:120261.
21. Huang Y, Li B, Liu D, Xie X, Zhang H, Sun H, Hu X, Zhang S. Fundamental Advances in Biomass Autothermal/Oxidative Pyrolysis: A Review. *ACS Sustain Chem Eng*. 2020; 8(32):11888–905.
22. Sato T, Sugime H, Noda S. CO_2-assisted growth of millimeter-tall single-wall carbon nanotube arrays and its advantage against H_2O for large-scale and uniform synthesis. *Carbon*. 2018; 136:143–9.
23. Hata K, Futaba DN, Mizuno K, Namai T, Yumura M, Iijima S. Water-assisted highly efficient synthesis of impurity-free single-walled carbon nanotubes. *Science*. 2004; 306(5700):1362–4.
24. Hasegawa K, Noda S. Millimeter-tall single-walled carbon nanotubes rapidly grown with and without water. *ACS Nano*. 2011; 5(2):975–84.
25. Yu B, Liu C, Hou PX, Tian Y, Li S, Liu B, Li F, Kauppinen EI, Cheng HM. Bulk synthesis of large diameter semiconducting single-walled carbon nanotubes by oxygen-

View Article Online
DOI: 10.1039/D5SC00768B

assisted floating catalyst chemical vapor deposition. *J Am Chem Soc*. 2011; 133(14):5232–5.
26. Oh T, Lee S. Optimization of steam-methane reforming process using PSA off gas. *Int J Hydrogen Energy*. 2024; 95:902–15.
27. Sun E, Zhai S, Kim D, Gigantino M, Haribal V, Dewey OS, et al. A semi-continuous process for co-production of CO_2-free hydrogen and carbon nanotubes via methane pyrolysis. *Cell Rep Phys Sci*. 2023 Apr 19;4(4):101338.
28. Cao A, Zhang X, Xu C, Liang J, Wu D, Wei B. Aligned carbon nanotube growth under oxidative ambient. *J Mater Res*. 2001; 16(11):3107–10.
29. Wang D, Wang K, Wu H, Luo Y, Sun L, Zhao Y, et al. CO_2 oxidation of carbon nanotubes for lithium-sulfur batteries with improved electrochemical performance. *Carbon*. 2018; 132:370–9.
30. Li JL, Kudin KN, McAllister MJ, Prud'homme RK, Aksay IA, Car R. Oxygen-driven unzipping of graphitic materials. *Phys Rev Lett*. 2006; 96(17):176101.
31. Xiangyun T, Guoquan L, Kuangdi X. Iron–Carbon Phase Diagram. *The ECPH Encyclopedia of Mining and Metallurgy*. 2023; 1–7.
32. Wirth CT, Bayer BC, Gamalski AD, Esconjauregui S, Weatherup RS, Ducati C, et al. The phase of iron catalyst nanoparticles during carbon nanotube growth. *Chemistry of Materials*. 2012; 24(24):4633–40.
33. Nishimura K, Okazaki N, Pan L, Nakayama Y. In situ study of iron catalysts for carbon nanotube growth using X-ray diffraction analysis. *Japanese Journal of Applied Physics, Part 2: Letters*. 2004; 43(4 A):L471.
34. Du Plessis HE, De Villiers JPR, Kruger GJ, Steuwer A, Brunelli M. Rietveld and pair distribution function study of Hägg carbide using synchrotron X-ray diffraction. *J Synchrotron Radiat*. 2011; 18(2):266–71.
35. He Z, Maurice JL, Gohier A, Lee CS, Pribat D, Cojocaru CS. Iron catalysts for the growth of carbon nanofibers: Fe, Fe_3C or both? *Chemistry of Materials*. 2011; 23(24):5379–87.
36. Li X, Cai W, Colombo L, Ruoff RS. Evolution of graphene growth on Ni and Cu by carbon isotope labeling. *Nano Lett*. 2009; 9(12):4268–72.
37. Pilipenko PS, Veselov VV. Carburization of metals with methane as a possible method for the low-temperature synthesis of iron, cobalt, and nickel carbides. *Soviet Powder Metallurgy and Metal Ceramics*. 1975;14(6):438–41.
38. Lan CC, Zhang SH, Liu XJ, Liu R, Lyu Q. Kinetic Behaviors of Coke Gasification with CO_2 and H_2O. *ISIJ International*. 2021;61(1):167–73.
39. Chang ZY, Wang P, Zhang JL, Jiao KX, Zhang YQ, Liu ZJ. Effect of CO_2 and H_2O on gasification dissolution and deep reaction of coke. *International Journal of Minerals, Metallurgy and Materials*. 2018; 25(12):1402–11.
40. Bhadeshia HKDH. Cementite. *International Materials Reviews*. 2020; 65(1):1–27.
41. Kukade S, Kumar P, Rao PVC, Choudary N V. Comparative study of attrition measurements of commercial FCC catalysts by ASTM fluidized bed and jet cup test methods. *Powder Technol*. 2016; 301:472–7.
42. Cocco R, Chew JW. 50 years of Geldart classification. *Powder Technol*. 2023; 428:118861.
43. Grande CA, Roussanaly S, Anantharaman R, Lindqvist K, Singh P, Kemper J. CO_2 Capture in Natural Gas Production by Adsorption Processes. *Energy Procedia*. 2017; 114:2259–64.

View Article Online
DOI: 10.1039/D5SC00768B

44. Hubbard R. The Role of Gas Processing in the Natural-Gas Value Chain. *Journal of Petroleum Technology*. 2009; 61(08):65–71.

View Article Online
DOI: 10.1039/D5SC00768B

Data availability

The authors declare that the data supporting the findings of this study are available within the article and the ESI.